HHS Public Access

Author manuscript

J Phys Chem B. Author manuscript; available in PMC 2018 June 15.

Published in final edited form as:

J Phys Chem B. 2017 June 15; 121(23): 5781–5793. doi:10.1021/acs.jpcb.7b00997.

Structural Properties of Nonionic Monorhamnolipid Aggregates in Water Studied by Classical Molecular Dynamics Simulations

Elango Munusamy, **Charles M. Luft**, **Jeanne E. Pemberton**, and **Steven D. Schwartz***

Department of Chemistry and Biochemistry, University of Arizona, Tucson, Arizona 85721, United States

Abstract

Molecular dynamics simulations were carried out to investigate the structure and stabilizing factors of aggregates of the nonionic form of the most common congener of monorhamnolipids, α-rhamnopyranosyl-β-hydroxydecanoyl-β-hydroxydecanoate (Rha-C10-C10), in water. Aggregates of size ranging from 5 to 810 monomers were observed in the simulation forming spherical and ellipsoidal structures, a torus-like structure, and a unilamellar vesicle. The effects of the hydrophobic chain conformation and alignment in the aggregate, role of monomer···monomer and monomer···water H-bonds, and conformations of monomers in the aggregate were studied in detail. The unilamellar vesicle is highly stable due to the presence of isolated water molecules inside the core adding to the binding energy. Dissociation of a monomer from a larger micellar aggregate is relatively easy compared to that from smaller aggregates as seen from potential of mean force calculations. This analysis also shows that monomers are held more strongly in aggregates of Rha-C10-C10 than the widely used surfactant sodium dodecyl sulfate. Comparisons between the aggregation behavior of nonionic and anionic forms of Rha-C10-C10 are presented.

Graphical abstract

* **Corresponding Author:** sschwartz@email.arizona.edu. Phone: 520-621-6363.

Supporting Information

The Supporting Information is available free of charge on the ACS Publications website at DOI: 10.1021/acs.jpcb.7b00997.
Free energy perturbation simulation details and results of aggregation of N40 and N20 to form a larger aggregate, N60 (Figures S1−S3), and force field parameters for monorhamnolipid (Figure S4) (PDF)
Rhamnolipid force field parameters (TXT)

ORCID

Elango Munusamy: 0000-0003-2389-7247
Jeanne E. Pemberton: 0000-0002-1710-2922
Steven D. Schwartz: 0000-0002-0308-1059

Notes

The authors declare the following competing financial interest(s): One author of this work (JEP) has equity ownership in GlycoSurf, LLC that is developing products related to the research being reported. The terms of this arrangement have been reviewed and approved by the University of Arizona in accordance with its policy on objectivity in research.

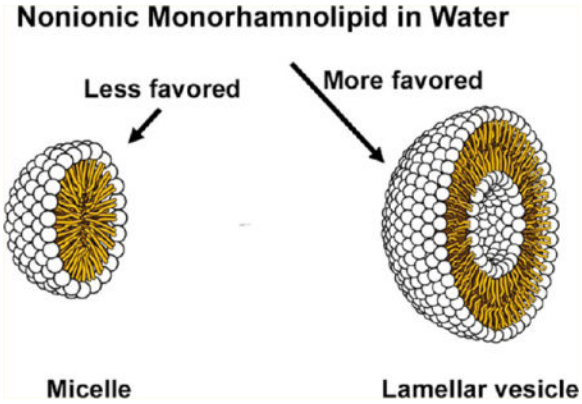

1. INTRODUCTION

Surfactants are an important class of amphiphilic molecules which lower the surface tension between two phases by accumulating at the interface. Surfactants find application in many different fields ranging from cleaning to food-processing, enhanced oil recovery, and the pharmaceutical sector. A majority of the available surfactants today are derived from petrochemical sources[1] and are only partially or slowly biodegradable, and as such, they contribute to environmental pollution. These compounds are often toxic to the environment, and their use may lead to significant ecological problems, particularly in cleaning applications as these surfactants inevitably end up in the environment after use.[2,3] The ecotoxicity, bioaccumulation, and biodegradability are therefore issues of increasing concern. Increasing environmental concern has led to a resurrection of industrial interest in biosurfactants, also known as surface-active agents of biological origin, due to their unique environmentally friendly properties and availability from renewable resources.

Biosurfactants have been studied by many research groups across the world, since the first biosurfactant “surfactin” was purified and characterized by Arima et al. in 1968.[4] There are as many as 250 patents obtained on these biodegradable molecules.[5,6] Biosurfactants are categorized by their chemical composition, molecular weight, physicochemical properties, mode of action, and microbial origin.[7] They are divided into low molecular mass biosurfactants, including glycolipids, phospholipids, and lipopeptides, and high molecular mass biosurfactants/bioemulsifiers containing amphipathic polysaccharides, proteins, lipopolysaccharides, lipoproteins, or complex mixtures of these biopolymers.[8–10] Low molecular mass biosurfactants are efficient in lowering surface and interfacial tension, whereas high molecular mass biosurfactants are more effective at stabilizing oil-in-water emulsions.

Among various categories of biosurfactants, the glycolipid biosurfactants “rhamnolipids” stand apart.[11] Rhamnolipid[12] is composed of a β-hydroxyalkanoyl-β-hydroxyalkanoic acid connected by the carboxyl end to a rhamnose sugar molecule. Rhamnolipids are produced by *Pseudomonos aeruginosa* and classified as monorhamnolipids (Scheme 1) and dirhamnolipids. Other *Pseudomonos* species that have been reported to produce rhamnolipids are *Pseudomonos chlororaphis*, *Pseudomonos plantarii*, *Pseudomonos putida*,

and *Pseudomonos fluorescens*. Some strains are known to produce only monorhamnolipids, while most produce both. The ratio of mono- and dirhamnolipids can also be controlled in the production method.

In the past three decades, there has been a large body of research work produced related to rhamnolipids, revealing many of their applications and causing them to reach significant use among all the categories of biosurfactants in the global market.[13–16] Rhamnolipids are stable over a wide range of temperatures and pressures, are nontoxic, and are themselves biodegradable. They contain only the common elements of carbon, hydrogen, and oxygen. During biodegradation, rhamnolipids are broken down into rhamnose sugars and common fatty acids that are easily metabolized. Rhamnolipids as a natural product have numerous applications. (i) *Agriculture and farming*: as a wetting and dispersal agent for the application of agricultural fungicides and pesticides. (ii) *Pharmaceutics*: to heal bedsores that have failed to respond to traditional treatments, in wound and burn treatment[17] accelerating the healing process and reducing the associated scarring that occurs with other remedies, and fighting fungal and bacterial infections. (iii) *Drug delivery*: since rhamnolipids can be used to form liposomes, there are potential applications for drug delivery. (iv) *Enhanced oil recovery*: it is estimated that only 40% of an oil reservoir can be removed by simple pump and flooding methods. This is due to viscosity and adhering to the substrate in the reservoir. Tests indicate that the surfactant and emulsifying properties of rhamnolipids can be used to recover an additional 40% of the remaining oil in a well.[18] This enhanced oil recovery (EOR) facilitates the doubling of the petroleum recoverable from an oil well over traditional methods in a much more environmentally friendly manner. (v) *Bioremediation*: a process used to clean soil or groundwater contaminated by heavy metals or petroleum products into nonhazardous substances. Rhamnolipids have been documented to bind metal ions from contaminated sources.[19–22] This binding to monorhamnolipids, called complexation, is effective for a whole range of metals, including cadmium, lead, and zinc. It has been shown that the more toxic metals listed above have some of the highest affinities for complexation by rhamnolipids.[23] Metal chelators such as EDTA, which bind to metals in soil, although effective, have been found to be a persistent organic pollutant.

Despite the extensive experimental research and literature available on rhamnolipids, the amount of theoretical study on rhamnolipids is limited. There is no detailed structural information on the aggregation of rhamnolipids in bulk water or at interfaces. The need for computational studies on rhamnolipids is high for the following reasons: They are not a simple surfactant with a hydrophilic (head) and hydrophobic (tail) group. The headgroup is spread across the molecule, and they possess two alkyl chains. Their properties in water and at interfaces are completely different from those of well-known surfactants such as sodium dodecyl surfate (SDS). SDS dissolves in water and forms micelle of size ~60 molecules, whereas rhamnolipids have no limitation in the size of aggregates that can be formed. They can form structures ranging from premicellar aggregates to micelles and lamellar vesicles. Therefore, structural insights will help promote understanding of their properties, and molecular dynamics (MD) simulation is an appropriate tool to address this issue.

In this study, an attempt has been made to predict the aggregation behavior and structural properties (i.e., micelle size, shape, and spatial distribution of different groups within the

micelle and hydrophilic and hydrophobic interactions) of the most common monorhamnolipid congener, α-rhamnopyranosyl-β-hydroxydecanoyl-β-hydroxydecanoate ((*R*,*R*)-Rha-C10-C10), under conditions in which it exists in the nonionic form using MD simulations. It is well-known that the pK_a of these rhamnolipids in aggregates is 5.5, which is around neutral, making many potential applications of these materials likely under conditions for which they are nonionic.[24] A combined experimental and computational study on the aggregation behavior of the anionic form has been submitted for publication in *Langmuir*.[25] The presence of charge on an atom in a molecule will not only affect the bonded atoms but also the interactions between them and with the surroundings. In this investigation, the aggregation behavior of the nonionic form is studied as an important comparison to understand the aggregate features. Extensive structural details on the premicelles, micelles, and lamellar vesicles are presented. The second goal of this study is to calculate the free energy of desorption of a surfactant monomer from the micelle, using MD simulations and potential of mean force (PMF) calculations along the surfactant escape coordinate using a weighted histogram analysis method (WHAM).

2. SIMULATION METHODS

2.1. Simulation of Rha−C10-C10 Aggregates

Force field parameters for Rha-C10-C10 were first generated with charge groups defined according to the functional groups present in the molecule. Parameters for Rha-C10-C10 were obtained from the CHARMM (Chemistry at Harvard Macromolecular Mechanics) General Force Field (version 2b8)[26] and optimized according to the CHARMM force field[27] parametrization procedure to better reproduce the properties of Rha-C10-C10 at a high level of ab initio calculations. To validate the force field parameters, MD simulations on Rha-C10-C10 at the air−water interface were carried out, and the predicted surface area per molecule is ~92 Å^2. The experimental surface area per molecule at the complete surface coverage is reported as ~117 ± 12 Å^2.[28] There is a good agreement between the experiment and calculations, which supports the performance of the force field.

An initial starting structure for the aggregate is needed. The initial coordinates of the simulation were obtained by randomly placing Rha-C10-C10 molecules in a cubical box using PACKMOL software.[29] These randomly distributed Rha-C10-C10 molecules were explicitly solvated using a cubic box of pre-equilibrated TIP3P water.[30] The size of the water box was chosen to be 10 × 10 × 10 nm^3 for aggregates ranging from N = 5 to N = 100 and 15 × 15 × 15 nm^3 for N = 285 and N = 810 aggregates. The placement of Rha-C10-C10 molecules inside the water box is done ensuring that a minimal distance of at least 1 nm between boundary water and the closest atom of the Rha-C10-C10 molecule in any direction. Solvent molecules were removed if they were within 0.28 nm of any heavy atoms of Rha-C10-C10.

MD simulations were conducted with periodic boundary conditions using NAMD 2.9.[31] A direct cutoff for nonbonded interactions of 1 nm, a switch function starting at 0.8 nm for cutoff of van der Waals interactions, and particle mesh Ewald[32] for long-range electrostatics were applied. The SHAKE algorithm[33] was used to constrain all bonds involving hydrogen atoms, and a time step of 1 fs was used for the MD integration. The temperature and

pressure were controlled respectively by the Langevin thermostat and the Nose−Hoover Langevin barostat[34,35] as implemented in NAMD. The system was first energy minimized, then heated to 300 K, and finally equilibrated under constant 1 atm pressure and temperature. During minimization, heating, and equilibration, no constraints were applied. To avoid computationally expensive long relaxation times and large systems, a method of simulated annealing was employed.[36] The following protocol, used to obtain unbiased initial conformations, consists of a three-stage, simulated annealing: (i) temperature rise from 300 to 400 K in 200 ps, (ii) constant high-temperature equilibration at 400 K for 800 ps, and (iii) slow cooling back to 300 K in 1 ns.

MD simulations were employed to gain insight into the structural properties of aggregates formed from Rha-C10-C10 molecules. To elucidate the dynamic nature of the Rha-C10-C10 aggregates, we embarked on an MD investigation of micelle formation and structural evolution. Table 1 presents the list of systems studied in this work, comprising 5−810 molecules of the most common congener in the native Rha-C10-C10 mixture in its neutral state. The aggregate with 10 monomers is referred to as N10 for discussion, and this nomenclature is followed for all other aggregates. The aggregates were equilibrated with constant temperature molecular dynamics. The equilibrium condition is identified by stable total energy, temperature, and pressure. A production run was performed on the fully equilibrated system to analyze the properties of the aggregates formed.

2.2. Umbrella Sampling

The equilibrated configuration at the end of an NPT trajectory was used as the initial structure for a steered molecular dynamics (SMD) pulling simulation to generate the initial configurations for umbrella sampling within each window. The center of mass (COM) distances between each Rha-C10-C10 and the rest of the aggregate were calculated, and the Rha-C10-C10 molecule with the shortest COM distance from the rest of the aggregate was selected and then pulled relatively rapidly away from the aggregate over a 30 ps time scale using a spring constant of 7 kJ^{-1} nm^{-2} and a pulling rate of 0.002 nm ps^{-1}. This pulling was carried out to create a set of starting configurations for the umbrella sampling windows; snapshots were taken from this fast pulling trajectory with uniform spacing of windows. A total of 40 windows were used with a spacing of 0.06 nm COM separation between them. In each window, a 15 ns MD simulation was performed for umbrella sampling. A harmonic force with a force constant of 20 kcal mol^{-1} nm^{-2} was applied for each umbrella sampling window. To generate the PMFs, WHAM was used.[37]

3. RESULTS AND DISCUSSION

3.1. Aggregation Number

Table 2 presents the size of aggregates formed in all the systems starting from a random placement of molecules in the water box. It is interesting to note that Rha-C10-C10 can form aggregates of any size irrespective of the number of molecules present in the initial simulation. The smallest aggregates are formed with 5, 8, 10, and 16 molecules. The next largest aggregates are observed for 20, 25, and 30 molecules. It is interesting to see that an

aggregation number close to ~40 (40, 42, and 44) is observed in the simulations. We also observe that large aggregates of sizes 80 and 100 are formed.

Figure 1 presents illustrative structures of the aggregates observed in the simulation. It is evident from the cross-sectional view of the aggregates that N5 to ~N40 have a hydrophobic density free from any hydrophilic atoms or water. However, the cross-section of N80 shows the presence of hydrophilic parts buried inside the hydrophobic density. This is also true in the case of N100. This indicates that these aggregates are not a simple aggregate where a hydrophobic core is enclosed by hydrophilic moieties. To make sure that this observation is not an accident, we simulated 4 different systems with 100 monomers distributed randomly. We made sure that the random distribution of the monomers is entirely different in all four cases, ranging from close placement to distant placement. Figure 2 presents the N100 aggregate structures along with their cross-sections. It is possible to see that these aggregates are a collective of multiple aggregates. The system where the monomers were placed farther apart, panel iv in Figure 2, results in two aggregates. Simulation of these aggregates for longer times does not help in bringing all the hydrophobic parts together. Even after 60 ns of simulation, hydrophilic regions were still observed between the hydrophobic density. These results on aggregates N5 to N100 show that Rha-C10-C10 does not form simple, stable micellar aggregates larger than ~N40. Free energy perturbation calculation results showed that formation of N60 from N40 + N20 is not favorable. The details and results of the FEP calculations are provided in the Supporting Information. It is important to mention here that results on the anionic Rha-C10-C10 aggregates in water showed that aggregates larger than N40 form elliptical and tubular structures.[25] MD simulations on the large number of anionic Rha-C10-C10 monomers showed that smaller aggregates are formed at first, and then simulation for a longer period results in long tubular aggregates where hydrophobic regions are enclosed by hydrophilic regions. Below, we show that bigger structures such as a torus-like aggregate and a unilamellar vesicle are possible for nonionic Rha-C10-C10.

3.2. Aggregate Size and Shape

The aggregates presented in Figure 1 are highly dynamic, although this is not easily pictured by visualization of various frames along the trajectory. Therefore, we used well-known working equations to understand the size and shape of these aggregates. A characteristic measurement of the micelle size is its radius, r_{m}. The radius of the micelle can be calculated using the following two equations:

$$r_{\mathrm{m}} = \sqrt{\frac{5}{3}} R_{\mathrm{g}} \quad (1)$$

$$R_{\mathrm{g}} = \sqrt{\frac{1}{N}\sum_{i=1}^{N}(|r_i| - \langle r \rangle)^2} \quad (2)$$

where R_g is the radius of gyration and $\langle r \rangle$ is the mean distance of the heavy atoms (r_i) from the micelle COM. R_g is defined as the root-mean-square distance of the object's components from its center of mass. Figure 3 presents the calculated r_m (with error bars) for all the single aggregates (anionic and nonionic) observed in the study. These data show that the smaller aggregates have a radius of <1.5 nm. Aggregates of size N20 to ~N40 have radii between 1.5 and 2.2 nm. It is interesting to see that the aggregate sizes presented in this work are similar to the sizes of the aggregates formed of anionic Rha-C10-C10.[25] It is very clear from the figure that nonionic Rha-C10-C10 does not form micellar aggregates larger than ~N40 whereas anionic Rha-C10-C10 can form micellar aggregates larger than ~N40. It should be noted that these radii are average values of all the structures along the trajectory. Hence, these data alone cannot categorize these aggregates as spherical, ellipsoidal, or cylindrical.

The shape of the aggregate can be characterized by examining the eccentricity (e), defined as

$$e = 1 - \frac{I_{\min}}{I_{\text{av}}} \quad (3)$$

where $I_{\min}$ is the moment of inertia along the x-, y-, or z-axis with the smallest magnitude and I_{av} is the average of all three moments of inertia. Figure 4 shows the eccentricity as a function of the population for the aggregates. For a function of the population for the aggregates. For a spherical object, the value of e is 0, so deviation from sphericity can be quantified by examining the eccentricity in addition to visual inspection of system snapshots. It is evident from the figure that the eccentricity distribution of the smaller aggregates, N5 and N8, is really wide and the shape is highly undefined. The eccentricity distribution of N10 and N16 shows that they have wider peaks close to e = 0.2, but narrower than those of N5 and N8. It is interesting to see that the aggregate N20 is nearly spherical with e = 0.1. N25 and N30 have peaks sharper than those of smaller aggregates but are ellipsoids. The aggregates of size ~N40 have eccentricity distributions that have sharp peaks indicating the higher stability and are more ellipsoidal. This indicates the aggregates presented in this section are more spherical for N20 and slowly deviate to ellipsoids with increasing aggregation number. On the other hand, anionic Rha-C10-C10 aggregates form tubular structures in addition to spherical and ellipsoidal aggregates as seen from the eccentricity data.[25]

3.3. Spatial Distributions of Chemical Groups

In this section, we study the distributions of the alkyl chains, rhamnose ring, and water molecules from the COM of the aggregates. The purpose of this analysis is to identify the dynamic stability of the aggregates in water on the basis of the hydrophobic core present in them. We take into consideration the fact that, for a surfactant with an alkyl chain, the radius of the spherical hydrophobic core cannot exceed the length (l) of the chain. There are two alkyl chains in the Rha-C10-C10 molecule, and the effective length of an alkyl chain is only seven carbons (Scheme 1). The length of a seven-carbon chain in an all-*trans* conformation is ~7.6 Å. Figure 5 presents the radial density plots constructed by calculating the distance of atoms (representing a group) from the aggregate's COM and counting the number of atoms in 0.1 unit wide shells around the COM. The hydrophobic core of the aggregate

should be completely free from water and hydrophilic atoms. It is evident from the figure that N10 has a hydrophobic radius of ~6 Å. It is not a stable aggregate, which was also supported by the eccentricity results. Although 10 monomers of Rha-C10-C10 can stay together in water, the resulting hydrophobic core is too weak to stabilize it, which is why this aggregate is highly dynamic. It is interesting to see that the hydrophobic radius of N20 and N25 is ~7−8 Å, which is the same as the length of the alkyl chain; therefore, it is a stable aggregate. N16 is an aggregate where a transition can be achieved in terms of stability with addition of a few monomers, as seen from the radius of the hydrophobic core close to the ~7 Å mark. It is important to mention here that similar results were predicted for the anionic Rha-C10-C10 aggregates.[25] Smaller aggregates of anionic Rha-C10-C10 are highly dynamic, and the radial water density plot clearly shows the existence of water molecules around ~5 Å from the COM of the aggregate. The water density appears around 7−8 Å for the aggregates N20 and larger. This shows that anionic and nonionic Rha-C10-C10 aggregates are similar in size, shape, and spatial distribution of atoms in the aggregates.

3.4. Accessible Surface Area

The structural properties of an aggregate can be analyzed by quantifying the accessible surface area (ASA). The method of Lee and Richards[38] was used to determine the SA of the aggregate available for interaction with water. In this technique, all of the water molecules are removed from the system and a probe molecule is rolled across the surface of the aggregate. The contact area is summed to quantify the total accessible area. A 1.6 Å theoretical probe was utilized to mimic a water molecule. With this method, it is also possible to separate the contact area contribution from the hydrophilic group and the hydrophobic group. The results of this analysis for anionic and nonionic forms are presented in Figure 6. It could be seen from the figure that aggregates of both forms of Rha-C10-C10 have identical ASA per monomer values. For the stable aggregates N20 to ~N40, the SA of the hydrophilic group exposed to water is more abundant than that of the hydrophobic groups, indicating very little of the hydrophobic core is exposed to water. In the case of smaller aggregates N5, N8, N10, and N16, it can be seen that the ASA of the hydrophobic group exposed to water is comparatively greater. This shows that smaller aggregates are loosely packed and their hydrophobic parts are easily accessible to water. It should be noted that the ASA per monomer decreases with increasing size of the aggregate. This is likely due to a closer packing of the Rha-C10-C10 hydrophilic parts with increasing aggregation size. A similar result is obtained for the anionic form of Rha-C10-C10, with the ASA per monomer for aggregates larger than N20 dropping below 1 nm^2, and the premicellar aggregates have hydrophobic parts more exposed to water than micellar aggregates.[25]

3.5. Hydrophobic Chain Conformation

The structure of Rha-C10-C10 as a surfactant is complicated with hydrophilic atoms spread across the molecule and by the fact that there are two hydrophobic chains. To understand the role of the hydrophobic chain conformation in the formation of aggregates, the average distance between the terminal carbon atom (C10) and the sixth carbon from it (C4, Scheme 1) was calculated for both alkyl chains along the trajectory. It should be noted that the effective length of an alkyl chain in Rha-C10-C10 is only seven carbons. For smaller aggregates, due to the hydrophobic effect, hydrocarbon chains fold to reduce interaction

with water. As the aggregate size increases, the hydrocarbon chains do not fold, as they are kept away from water molecules by the hydrophilic exterior. The average chain length is ~6.8 Å, and this value is slightly less than the 7.6 Å calculated for a linear alkane of the same length (Scheme 1) in an all-*trans* conformation, suggesting some slight twisting along the chain axis. Further scrutiny of the results was made in the following way: The chain lengths are calculated and categorized into four groups, as bent (l < 5 Å), normal (l > 7 Å), and two intermediates (l = 5−6 Å, l = 6−7 Å). This classification is an attempt to understand the role of the chain conformation in the formation of the aggregate. The plot presented in Figure 7 shows that the percentage of fully "bent" chains is minimal in all the aggregates. A vast majority of the chains are in the "intermediate" state, l = 6−7 Å. A closer look at the distribution (Figure 7c) shows that the percentage of "normal" chains increases largely due to the decrease in the "intermediate" chain population as the aggregate size increases. Although the variation is only 5%, it is evident that the chains are more extended in larger aggregates than the smaller ones.

3.6. Headgroup Conformation

The Rha-C10-C10 molecule has polar carboxylic, hydroxyl, and ester groups that have a tendency to form intramolecular H-bonds. The intramolecular H-bonding distances between the carboxylic acid group and the rhamnose ring were calculated to understand the conformations of the headgroups in the aggregates. All possible intramolecular H-bonds as depicted in Scheme 2 were calculated by measuring the distance between the electronegative (oxygen) atoms. The shortest value among all possible interactions is chosen for an observed conformation and plotted for analysis. These H-bonds are denoted as $d_{O\cdots O}$ for the discussion. Here we have classified the conformations of Rha-C10-C10 on the basis of the value of $d_{O\cdots O}$ into four categories, folded ($d_{O\cdots O}$ < 5 Å), partially folded ($d_{O\cdots O}$ = 5−8 Å), partially open ($d_{O\cdots O}$ = 8−11 Å), and open ($d_{O\cdots O}$ > 11 Å). Figure 8a shows the representative conformations of Rha-C10- C10 in all four categories. The calculated population shows that ~20% of Rha-C10-C10 molecules are in the folded conformation. The majority of the molecules are in the partially folded and partially open conformations. The figure shows that less than 10% of the monomers are in open conformations. This indicates that Rha-C10-C10 molecules prefer partially open/folded conformations in the aggregates.

3.7. Contribution of H-Bonding to the stability

To understand the role of H-bonding in the stability of the aggregates, we analyzed all the possible H-bonds present in the system. We considered two types of H-bonds for discussion: (i) (Rha-C10-C10)⋯(Rha−C10-C10) refers to H-bonding between monomers constituting the aggregate; (ii) (Rha-C10-C10) ⋯water refers to H-bonding between monomers and the water molecules. H-bonds were identified using the cutoff conditions that H-bond distances between electronegative atoms are ≤3.0 Å and H-bond O−O−H angles are ≤20°. It is clear from Figure 9 that the number of (Rha-C10-C10)⋯(Rha-C10-C10) H-bonds is very small for the nonionic form. There is 0.3 H-bond per monomer for the aggregate ~N40. Although there is a slight increase in H-bonding with aggregate size, it is not significant. The (Rha-C10-C10)⋯water H-bond results predict that each monomer forms H-bonds with approximately three water molecules. These results clearly show that the formation and stability of the nonionic Rha-C10-C10 aggregates of size N5 to ~N40 do not come from

(Rha-C10-C10)···(Rha-C10-C10) H-bonds. Considering the fact that the effective alkyl chain length is only seven carbons, one would expect an extra stabilization in the form of a (Rha-C10-C10)···(Rha-C10-C10) H-bonding network would be necessary to stabilize the aggregate formation in addition to the hydrophobic effect. However, this is not the case here, and the majority of the stability within the aggregates is expected from hydrophobic chain interactions. This could be one of the reasons for not observing micellar aggregates larger than ~N40. It is evident from the figure that the anionic Rha-C10-C10 aggregates differ from nonionic Rha-C10-C10 aggregates with respect to the H-bonding. The anionic Rha-C10-C10 molecule makes the H-bonding present in these aggregates much stronger (gas-phase density functional theory (DFT) calculations show a 4-fold increase in strength for $O^{-}\cdots H-O$ compared to O···H−O interactions).[25,39] This is evident from the (Rha-C10-C10) ···(Rha-C10-C10) H-bonds per monomer values, ~0.5 for N20 and ~1 for N40. Also there is 3-fold increase in water molecules forming H-bonds with the surfactant. This is the major reason for observing micellar aggregates larger than ~N40 in the anionic Rha-C10-C10.

3.8. Alignment of the Alkyl Chains

It is evident from the previous section that the stability of Rha-C10-C10 aggregates N5 to N40 in water is largely due to hydrophobic interactions. The presence of two alkyl chains makes the Rha-C10-C10 molecule interesting in terms of hydrophobic density, so the alignment of the two chains in the aggregate is important. Thus, we studied the distribution of the alignment of the alkyl chains in the aggregates. The alkyl chains of Rha-C10-C10 are held static at one end and are free to move on the other end (Scheme 1). It is not straightforward to understand the alignment of the chains in all of the molecules in the aggregate for the entire trajectory. Therefore, we used the distance between two carbon atoms, one from each chain, as a proxy for this property of alignment. Figure 10b presents the structure of monomers with varying alignment of the alkyl chains based on the distance $d_{C10\cdots C10}$. It is clear from the figure that alignment of the alkyl chains in a molecule is broadly distributed. In Figure 10a we present the population of C···C distances $d_{C10\cdots C10}$, $d_{C8\cdots C8}$, and $d_{C6\cdots C6}$. It is seen from the plot that the major population of monomers have alkyl chains that are closer to each other by ~6 Å, which could be treated as parallel. A smaller population of monomers have chains that deviate significantly from parallel. Therefore, the aggregates have a combination of parallel and unparallel alignment of alkyl chains.

3.9. Unilamellar Vesicle and Torus Aggregate

The absence of micellar aggregates bigger than ~N40 created an interest to study larger aggregates. In this regard, we studied a torus-like aggregate and a unilamellar vesicle (ULV) of Rha-C10-C10. ULVs are of great practical interest due to their potential use in nano- and biotechnology for encapsulation and delivery of drug molecules. From a fundamental point of view, ULVs are thought to be an idealistic representation of a cell membrane. As a result, extensive studies have been carried out to describe their structures in equilibrium. Rhamnolipids are known to form liposomes, which are referred to as open or closed vesicles. We have performed MD simulations on a torus-like aggregate with 285 monomers and a ULV with 810 monomers. The process of formation of ULVs usually involves different stages with certain rate-limiting steps, creating kinetics spanning from milliseconds

to days, depending on the type of surfactant employed and the type of transformation taking place. The limitation associated with the size of the simulation system, a larger time scale, led us to create a preassembled torus-like aggregate and a ULV. We used PACKMOL software to generate the starting structure and a larger simulation water box (15 × 15 × 15 nm^3) for solvation. The representative snapshots of N285 and N810 are shown in Figure 11. A cross-section of the ULV is also shown in the figure to show the presence of water molecules inside the ULV. The calculated radius of the ULV is 6 nm. It is highly stable and spherical in shape as seen from the sharp peak of the eccentricity distribution near $e = 0.1$ shown in Figure 11e. The inner core of the ULV holds ~2500 water molecules isolated from the rest of the bulk water. These water molecules could be used to solvate hydrophilic drug molecules for drug delivery applications. The intramolecular H-bonding between monomers present in the ULV is calculated as 0.4 per monomer. This result shows that H-bonds between monomers of the aggregate do not contribute significantly to the stabilization of the aggregate as observed in the case of N5 to ~N40 aggregates. The H-bonding interaction of the ULV with water shows that there are 2.2 water molecules H-bonded to a monomer. The tight packing of the hydrophilic parts of the monomers in the ULV makes way for fewer water molecules to interact with them than in loosely packed smaller aggregates. These results show the stabilization of the ULV might be due to isolated water molecules in the core holding the entire structure together and the hydrophobic interactions. The thickness of the hydrophobic region is measured by plotting the water density, radially from the COM of the ULV. Figure 11f shows that the average thickness of the hydrophobic bilayer is ~16 Å, which is roughly twice the length of the seven-carbon alkane. We conclude, therefore, that the higher stability of the ULV comes from two factors: (i) the water buried inside the core of the ULV and (ii) the thick hydrophobic bilayer.

3.10. Energetics of Monomer Removal

Micelles are often drawn as static spherical structures of oriented surfactant molecules. However, they are in dynamic equilibrium with individual surfactant molecules that are constantly being exchanged with the bulk water. They also continuously disintegrate and re-form themselves. Two relaxation processes are believed to be involved with surfactants in solutions. First is the fast relaxation time which is associated with the fast exchange of monomers between aggregates and the surrounding medium. The second relaxation time is attributed to aggregate formation and the dissolution process. These relaxation kinetics are important to several interfacial processes, such as foaming, antifoaming, wetting, emulsification, solubilization, and detergency.[40,41]

In this section, we calculate the free energy of desorption of a monomer from an aggregate using umbrella sampling[42] and WHAM. A single Rha-C10-C10 molecule is pulled away from the rest of the aggregate, and the associated PMF is calculated during this process. The PMFs calculated using an in-house WHAM code are shown in Figure 12a for aggregates N30 and N40. It is interesting to see that the minimum of the PMF occurs at $r \approx 15$ Å for N30 and $r \approx 18$ Å for N40. These values are comparable to the calculated R_g values of the aggregates, 14.0 Å for N30 and 16.6 Å for N40, and they are the most probable locations for a monomer in the aggregates. It is possible to see from the figure that above $R \approx 27$ Å and $R \approx 32$ Å, the PMFs are flat with an increasing value of R. This shows that the monomer that

just escaped from the aggregate is unstable until it merges into another aggregate close by. Parts b and c of Figure 12 present the corresponding structures showing the monomer just about to leave the aggregate. The heights of the PMF at these escape points are ~8 and ~6 kcal/ mol for N30 and N40, respectively. This indicates that larger aggregates more easily allow monomers to dissociate into the bulk solution, whereas it is relatively difficult to pluck a monomer from the smaller aggregates. It should be noted that the PMF values reported here are larger than those reported for removal of an SDS monomer from an aggregate (~5 kcal/mol for an optimal aggregation size of 60 monomers).[43,44] The structural differences between SDS and Rha-C10-C10 support this observation. The headgroup in SDS, $-OSO_3^-$, is small, and the negative charge is delocalized between the three oxygens. There exists a repulsive interaction between the headgroups which supports the expulsion of a monomer from the aggregate. On the other hand, the Rha-C10-C10 headgroup is spread across the molecule, and a H-bonding interaction is possible between the monomers, which acts against the removal of a monomer. It is also important to mention here that the presence of two alkyl chains in Rha-C10-C10, although shorter than the single alkyl chain in SDS, makes it harder to pull a monomer from an aggregate in the former rather than the latter.

4. CONCLUSIONS

Molecular dynamics simulations were carried out on a series of systems containing nonionic Rha-C10-C10 of size 5−810 molecules. The results of the present study were compared with those of the anionic Rha-C10-C10 to understand the aggregation properties arising from structural differences. The following are the salient features that emerge from the current study: (1) Nonionic Rha-C10-C10 can form aggregates of size as small as 5 molecules to a very large number in shape ranging from spherical to ellipsoidal, torus-like, and unilamellar vesicle. A critical analysis of these aggregates shows that the aggregation number does not exceed ~40 for micellar aggregates, i.e., a single hydrophobic core surrounded by hydrophilic headgroups. Anionic Rha-C10-C10 can form micellar aggregates larger than ~N40. (2) The eccentricity study shows that the shape of the nonionic Rha-C10-C10 aggregates changes from spherical to ellipsoidal with increasing aggregation number. Anionic Rha-C10-C10 can form long tubular structures in addition to spherical and ellipsoidal structures. (3) The alkyl chains of the monomer are bent in smaller aggregates and are more extended in larger aggregates. (4) The headgroup conformations in the aggregate are mostly open with a small percentage in the folded state in which the carboxylic acid group forms intramolecular H-bonds with the hydroxyl group of the rhamnose ring. (5) The alkyl chains of a monomer are aligned parallel to each other in the aggregate in most cases. (6) Anionic (Rha-C10-C10)···(Rha-C10-C10) H-bonding interaction is much stronger than nonionic (Rha-C10-C10) ···(Rha-C10-C10) H-bonding. As a result, the H-bonding interaction between nonionic (Rha-C10-C10)···(Rha-C10-C10) does not contribute significantly to the stability of the aggregate. (7) The H-bonding interaction of the monomers and water ((Rha-C10-C10)···water) in the anionic and nonionic forms shows that a monomer interacts with ~9 and ~3 water molecules, respectively. (8) A lack of (Rha-C10-C10)···(Rha-C10-C10) H-bonding and the effective alkyl chain length being shorter restrict the population of micellar structures larger than ~N40. Stronger anionic (Rha-C10-C10)···(Rha-C10-C10) H-bonding supports the formation of micellar structures larger than

~N40 despite the shorter alkyl chain. (9) The torus-like aggregate and unilamellar vesicles are highly stable with a strong hydrophobic bilayer. ULVs have additional stability from the constrained water molecules present inside them. (10) Umbrella sampling calculations show that larger aggregates more easily exchange monomers with the bulk than smaller aggregates. These extensive structural analyses of the Rha-C10-C10 aggregates in water show how different and complicated they are compared to the simplest surfactants such as SDS with a compact headgroup and a single-chain tail. The structures of Rha-C10-C10 are responsible for the range of aggregates that can be formed in water. Several structural factors act together to give Rha-C10-C10 these unique properties.

Acknowledgments

We gratefully acknowledge support of this research through a grant award from the National Science Foundation (CHE-1339597) jointly funded by the Environmental Protection Agency as part of the Networks for Sustainable Molecular Design and Synthesis Program.

References

1. Van Bogaert IN, Saerens K, De Muynck C, Develter D, Soetaert W, Vandamme EJ. Microbial Production and Application of Sophorolipids. Appl Microbiol Biotechnol. 2007; 76:23–34. [PubMed: 17476500]
2. Mann RM, Boddy MR. Biodegradation of a Nonylphenol Ethoxylate by the Autochthonous Microflora in Lake Water with Observations on the Influence of Light. Chemosphere. 2000; 41:1361–9. [PubMed: 11057572]
3. Mann RM, Bidwell JR. The Acute Toxicity of Agricultural Surfactants to the Tadpoles of Four Australian and Two Exotic Frogs. Environ Pollut. 2001; 114:195–205. [PubMed: 11504342]
4. Arima K, Kakinuma A, Tamura G. Surfactin, a Crystalline Peptidelipid Surfactant Produced by Bacillussubtilis: Isolation, Characterization and Its Inhibition of Fibrin Clot Formation. Biochem Biophys Res Commun. 1968; 31:488–494. [PubMed: 4968234]
5. Shete AM, Wadhawa G, Banat IM, Chopade BA. Mapping of Patents on Bioemulsifier and Biosurfactant: A Review. J Sci Ind Res. 2006; 65:91–115.
6. Rahman PKSM, Gakpe E. Production, Characterisation and Applications of Biosurfactants-Review. Biotechnology. 2008; 7:360–370.
7. Abdel-Mawgoud AM, Lépine F, Déziel E. Rhamnolipids: Diversity of Structures, Microbial Origins and Roles. Appl Microbiol Biotechnol. 2010; 86:1323–1336. [PubMed: 20336292]
8. Müller MM, Kügler JH, Henkel M, Gerlitzki M, Hörmann B, Pöhnlein M, Syldatk C, Hausmann R. Rhamnolipids—Next Generation Surfactants? J Biotechnol. 2012; 162:366–380. [PubMed: 22728388]
9. Banat IM, Makkar RS, Cameotra SS. Potential Commercial Applications of Microbial Surfactants. Appl Microbiol Biotechnol. 2000; 53:495–508. [PubMed: 10855707]
10. Zhang L, Veres-Schalnat TA, Somogyi A, Pemberton JE, Maier RM. Fatty Acid Cosubstrates Provide Beta-Oxidation Precursors for Rhamnolipid Biosynthesis in Pseudomonas Aeruginosa, as Evidenced by Isotope Tracing and Gene Expression Assays. Appl Environ Microbiol. 2012; 78:8611–8622. [PubMed: 23042167]
11. Dobler L, Vilela LF, Almeida RV, Neves BC. Rhamnolipids in Perspective: Gene Regulatory Pathways, Metabolic Engineering, Production and Technological Forecasting. New Biotechnol. 2016; 33:123–135.
12. Burger MM, Glaser L, Burton RM. The Enzymatic Synthesis of a Rhamnose-Containing Glycolipid by Extracts of Pseudomonas Aeruginosa. J Biol Chem. 1963; 238:2595–2602. [PubMed: 14063278]
13. Abdel-Mawgoud AM, Lepine F, Deziel E. Rhamnolipids: Diversity of Structures, Microbial Origins and Roles. Appl Microbiol Biotechnol. 2010; 86:1323–36. [PubMed: 20336292]

14. Jirku V, Cejkova A, Schreiberova O, Jezdik R, Masak J. Multicomponent Biosurfactants–a “Green Toolbox” Extension. Biotechnol Adv. 2015; 33:1272–6. [PubMed: 25773671]
15. Lovaglio RB, Silva VL, Ferreira H, Hausmann R, Contiero J. Rhamnolipids Know-How: Looking for Strategies for Its Industrial Dissemination. Biotechnol Adv. 2015; 33:1715–26. [PubMed: 26384475]
16. Marchant R, Banat IM. Biosurfactants: A Sustainable Replacement for Chemical Surfactants? Biotechnol Lett. 2012; 34:1597–605. [PubMed: 22618240]
17. Stipcevic T, Piljac A, Piljac G. Enhanced Healing of Full-Thickness Burn Wounds Using Di-Rhamnolipid. Burns. 2006; 32:24–34. [PubMed: 16380213]
18. Banat IM. Biosurfactants Production and Possible Uses in Microbial Enhanced Oil Recovery and Oil Pollution Remediation: A Review. Bioresour Technol. 1995; 51:1–12.
19. Ochoa-Loza FJ, Artiola JF, Maier RM. Stability Constants for the Complexation of Various Metals with a Rhamnolipid Biosurfactant. J Environ Qual. 2001; 30:479–485. [PubMed: 11285908]
20. Hogan, D., Veres-Schalnat, T., Pemberton, J., Maier, R. Biosurfactants. CRC Press; Boca Raton, FL: 2013. Biosurfactant Complexation of Metals and Applications for Remediation; p. 277-308.
21. Herman DC, Artiola JF, Miller RM. Removal of Cadmium, Lead, and Zinc from Soil by a Rhamnolipid Biosurfactant. Environ Sci Technol. 1995; 29:2280–2285. [PubMed: 22280267]
22. Tan H, Champion JT, Artiola JF, Brusseau ML, Miller RM. Complexation of Cadmium by a Rhamnolipid Biosurfactant. Environ Sci Technol. 1994; 28:2402–2406. [PubMed: 22176061]
23. Dahrazma B, Mulligan CN. Investigation of the Removal of Heavy Metals from Sediments Using Rhamnolipid in a Continuous Flow Configuration. Chemosphere. 2007; 69:705–711. [PubMed: 17604818]
24. Lebron-Paler A, Pemberton JE, Becker BA, Otto WH, Larive CK, Maier RM. Determination of the Acid Dissociation Constant of the Biosurfactant Monorhamnolipid in Aqueous Solution by Potentiometric and Spectroscopic Methods. Anal Chem. 2006; 78:7649–58. [PubMed: 17105155]
25. Eismin RJ, Elango M, Kegel LL, Hogan DE, Maier RM, Schwartz SD, Pemberton JE. Evolution of Aggregate Structure in Solutions of Anionic Monorhamnolipids: Experimental and Computational Results. Langmuir. 2017 submitted for publication.
26. Vanommeslaeghe K, et al. CHARMM General Force Field: A Force Field for Drug-Like Molecules Compatible with the CHARMM All-Atom Additive Biological Force Fields. J Comput Chem. 2010; 31:671–690. [PubMed: 19575467]
27. Best R, Zhu X, Shim J, Lopes P, Mittal J, Feig M, MacKerell A. Optimization of the Additive Charmm All-Atom Protein Force Field Targeting Improved Sampling of the Backbone Phi, Psi and Side-Chain Chi(1) and Chi(2) Dihedral Angles. J Chem Theory Comput. 2012; 8:3257–3273. [PubMed: 23341755]
28. Palos Pacheco R, Eismin RJ, Coss CS, Wang H, Maier RM, Polt R, Pemberton JE. Synthesis and Characterization of Four Diastereomers of Monorhamnolipids. J Am Chem Soc. 2017; 139:5125–5132.
29. Martinez L, Andrade R, Birgin E, Martinez J. Packmol: A Package for Building Initial Configurations for Molecular Dynamics Simulations. J Comput Chem. 2009; 30:2157–2164. [PubMed: 19229944]
30. Jorgensen W, Chandrasekhar J, Madura J, Impey R, Klein M. Comparison of Simple Potential Functions for Simulating Liquid Water. J Chem Phys. 1983; 79:926–935.
31. Phillips J, Braun R, Wang W, Gumbart J, Tajkhorshid E, Villa E, Chipot C, Skeel R, Kale L, Schulten K. Scalable Molecular Dynamics with Namd. J Comput Chem. 2005; 26:1781–1802. [PubMed: 16222654]
32. Darden T, York D, Pedersen L. Particle Mesh Ewald - an N.Log(N) Method for Ewald Sums in Large System. J Chem Phys. 1993; 98:10089–10092.
33. Ryckaert J, Ciccotti G, Berendsen H. Numerical-Integration of Cartesian Equations of Motion of a System with Constraints -Molecular-Dynamics of N-Alkanes. J Comput Phys. 1977; 23:327–341.
34. Martyna G, Tobias D, Klein M. Constant-Pressure Molecular-Dynamics Algorithms. J Chem Phys. 1994; 101:4177–4189.
35. Feller S, Zhang Y, Pastor R, Brooks B. Constant-Pressure Molecular-Dynamics Simulation - the Langevin Piston Method. J Chem Phys. 1995; 103:4613–4621.

36. Kirkpatrick S, Gelatt C, Vecchi M. Optimization by Simulated Annealing. Science. 1983; 220:671–680. [PubMed: 17813860]

37. Kumar S, Rosenberg JM, Bouzida D, Swendsen RH, Kollman PA. The Weighted Histogram Analysis Method for Free-Energy Calculations on Biomolecules. I. The Method. J Comput Chem. 1992; 13:1011–1021.

38. Lee B, Richards F. Interpretation of Protein Structures -Estimation of Static Accessibility. J Mol Biol. 1971; 55:379–400. [PubMed: 5551392]

39. Parthasarathi R, Subramanian V, Sathyamurthy N. Hydrogen Bonding without Borders: An Atoms-in-Molecules Perspective. J Phys Chem A. 2006; 110:3349–3351. [PubMed: 16526611]

40. Patist A, Jha BK, Oh SG, Shah DO. Importance of Micellar Relaxation Time on Detergent Properties. J Surfactants Deterg. 1999; 2:317–324.

41. Patist A, Kanicky JR, Shukla PK, Shah DO. Importance of Micellar Kinetics in Relation to Technological Processes. J Colloid Interface Sci. 2002; 245:1–15. [PubMed: 16290329]

42. Kastner J. Umbrella Sampling. Wires Comput Mol Sci. 2011; 1:932–942.

43. Yuan F, Wang S, Larson RG. Potentials of Mean Force and Escape Times of Surfactants from Micelles and Hydrophobic Surfaces Using Molecular Dynamics Simulations. Langmuir. 2015; 31:1336–1343. [PubMed: 25560633]

44. Li Z, Fichthorn KA, Milner ST. Surfactant Binding to Polymer−Water Interfaces in Atomistic Simulations. Langmuir. 2016; 32:7519–7529. [PubMed: 27347809]

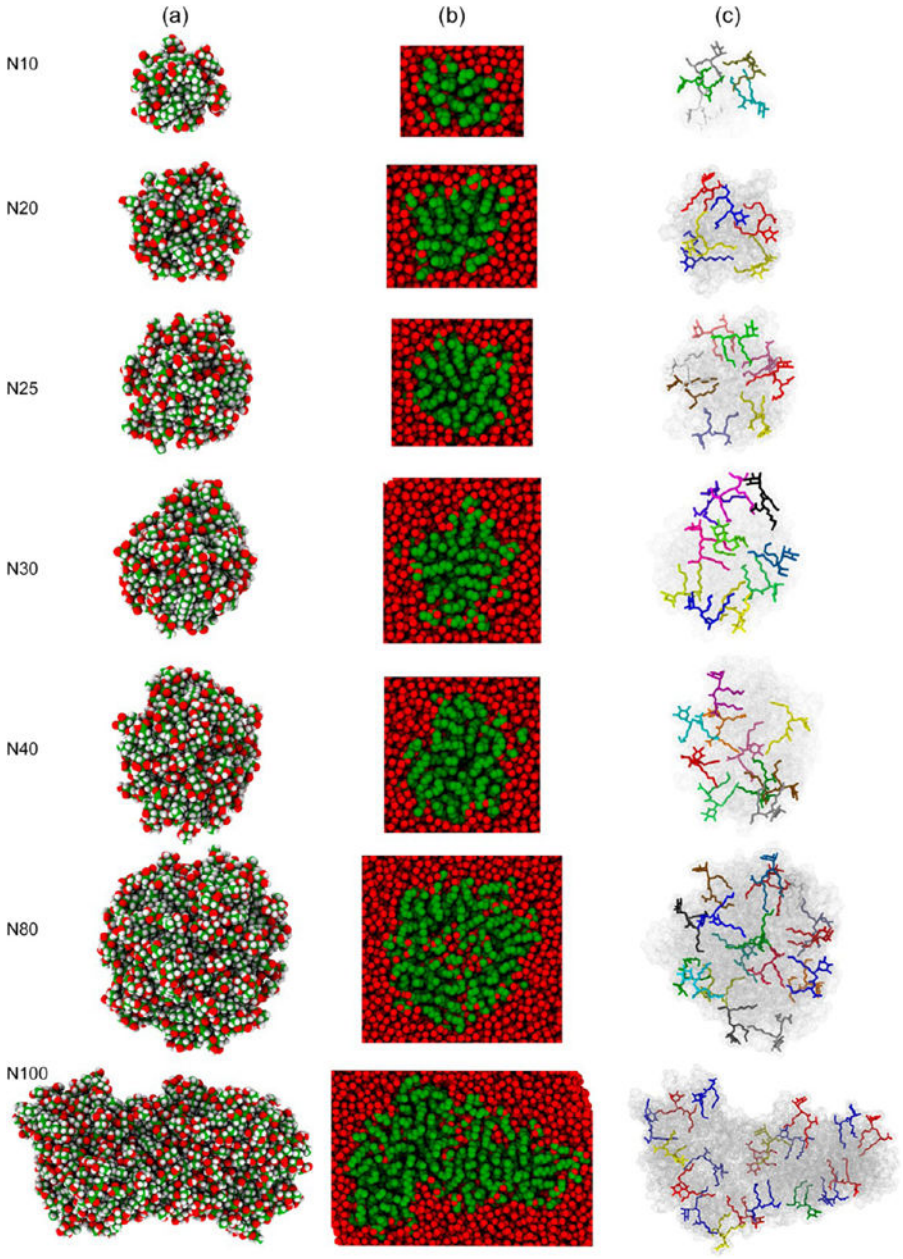

Figure 1.

Snapshot of the Rha-C10-C10 aggregates obtained from the MD simulations. (a) Sphere model of aggregates showing their shape. For a clear presentation water molecules are not shown. (b) Cross-sectional view of the aggregates in water. Red spheres are oxygen, and green spheres are carbon. (c) Orientation of Rha-C10-C10 molecules in the aggregates. Different colors are used for a better view of the monomers.

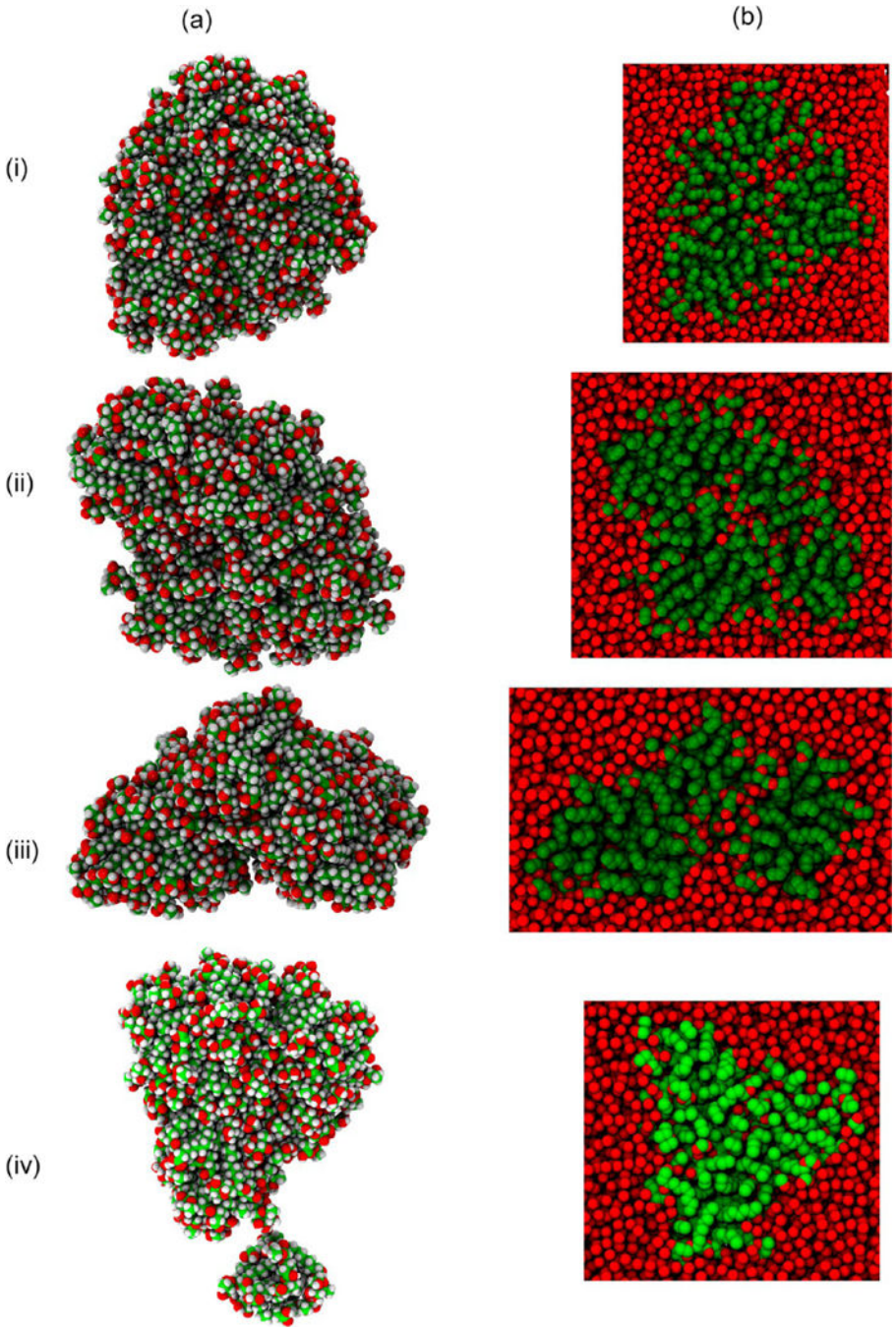

Figure 2.

(a) Snapshots and (b) cross-section of N100 aggregates obtained starting from different initial structures.

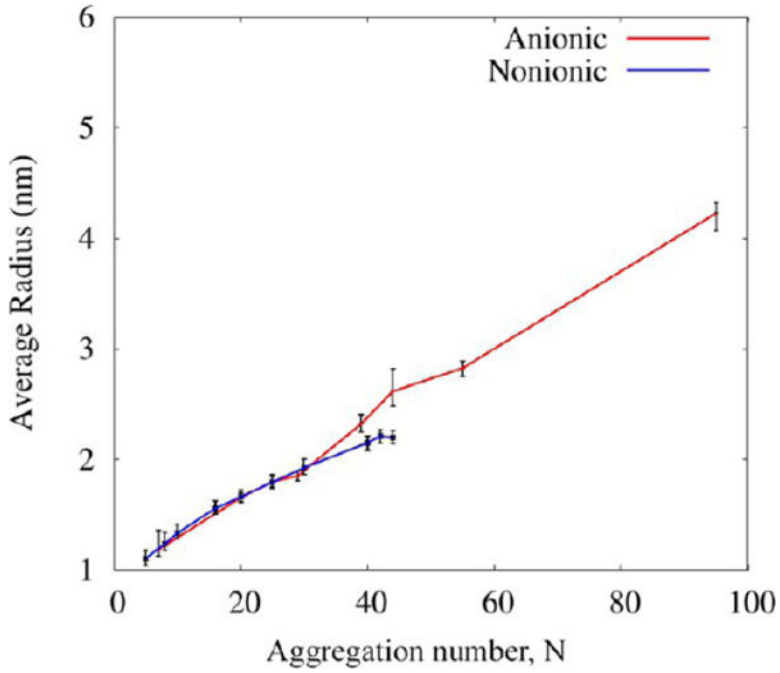

Figure 3.

Average radius (with error bars) vs number of Rha-C10-C10 molecules for all the aggregates observed in the MD simulations. The average radius is calculated from all structures along the trajectory.

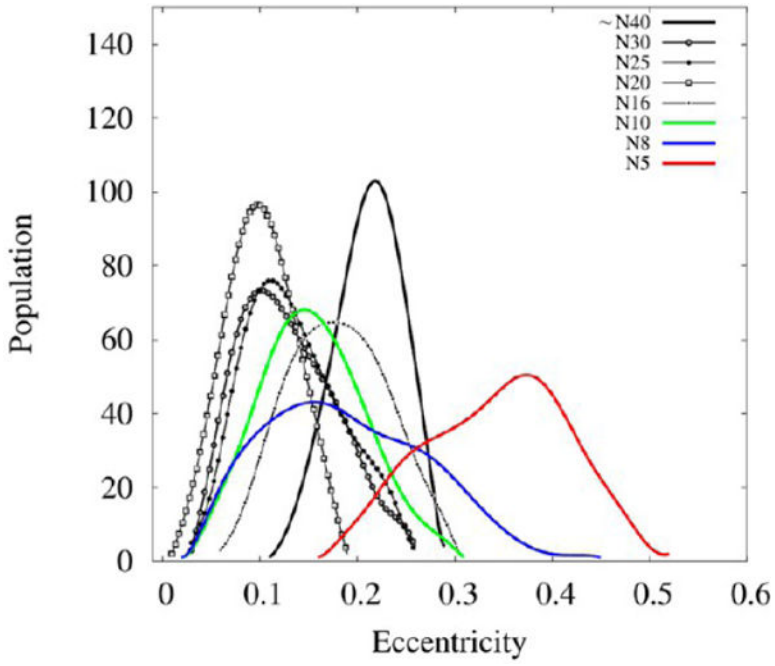

Figure 4.
Population distribution of eccentricities of different aggregates observed in the study.

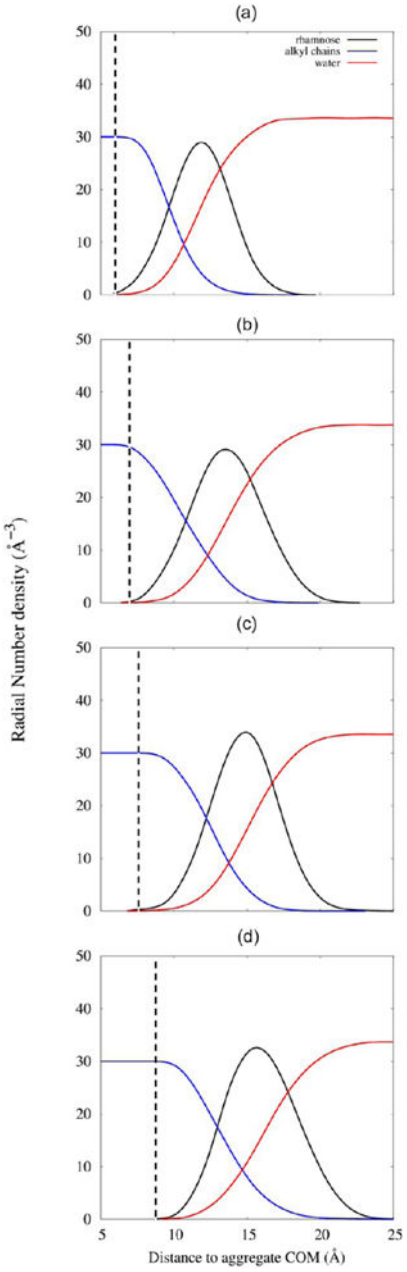

Figure 5.

Radial number density of the rhamnose group, alkyl chains, and water from the center of mass for aggregates (a) N10, (b) N16, (c) N20, and (d) N25. The dotted vertical line indicates the radius of the hydrophobic core which is completely free from hydrophilic atoms and water.

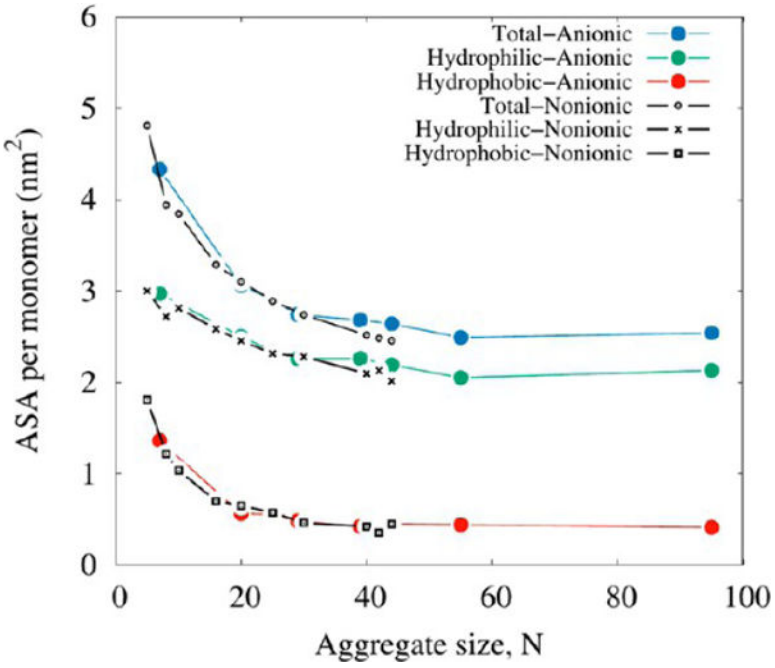

Figure 6.

Solvent-accessible surface area per monomer as a function of the number of monomers in the aggregate. The surface areas that correspond to the hydrophilic and hydrophobic atoms are also presented.

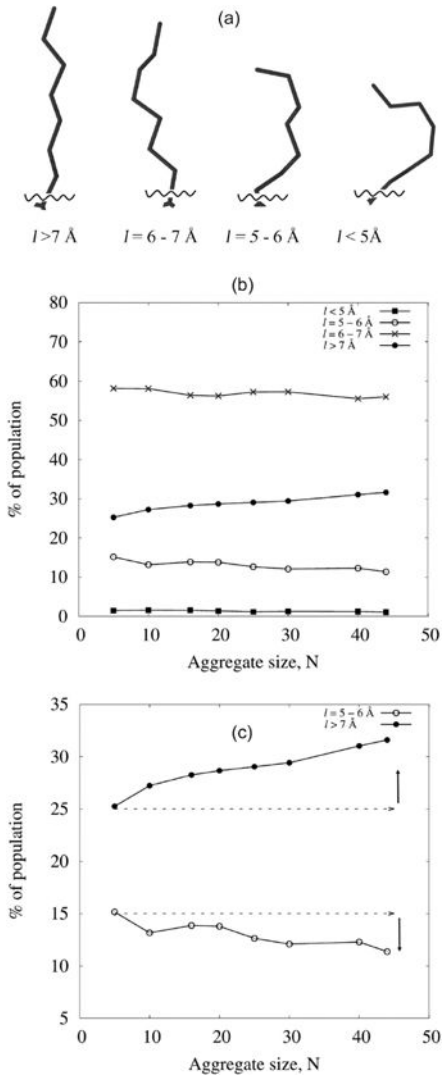

Figure 7.

(a) Representative structure of the alkyl chain showing the extent of bending. (b) Distribution of the extent of bent/relaxed alkyl chains in all of the aggregates observed in the simulation. (c) Close examination of the change in the population of bent/relaxed alkyl chain as a function of the aggregate size.

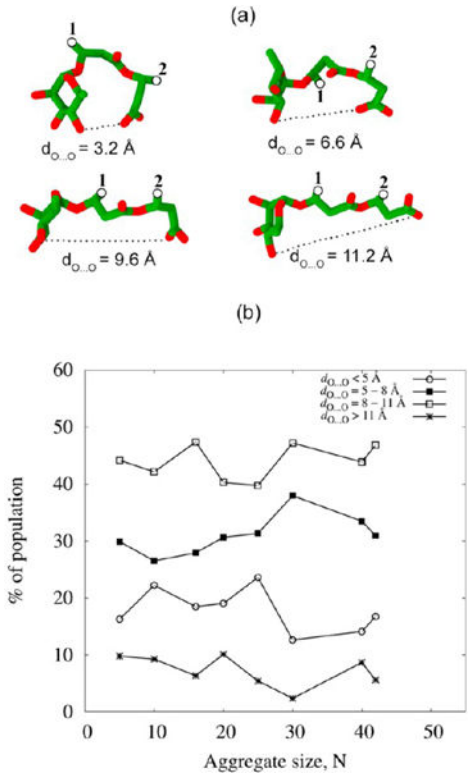

Figure 8.

(a) Representative structure of Rha-C10-C10 in different conformations. The alkyl chains (shown as 1 and 2) are represented with a hollow circle, and hydrogen atoms are omitted for clarity. (b) Percentages of different conformations of Rha-C10-C10 in all of the aggregates observed in the simulation.

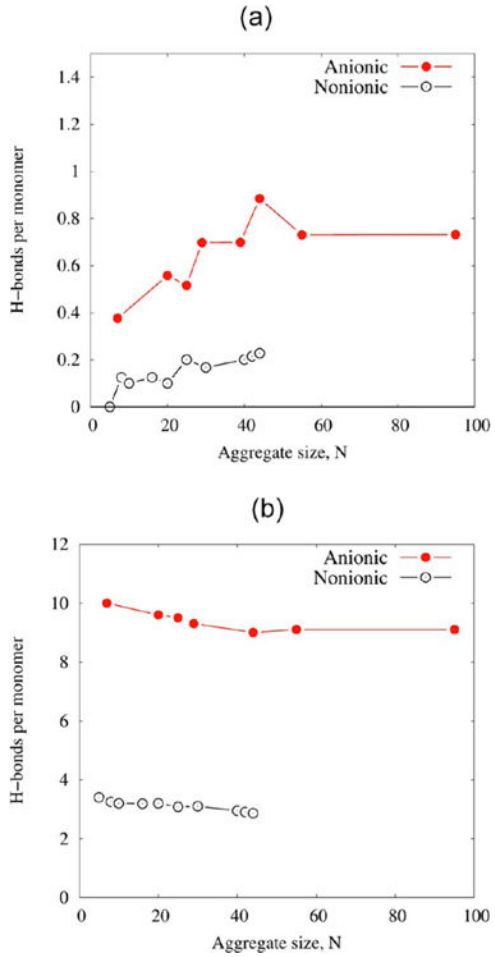

Figure 9.

Number of H-bonds per monomer for (a) (Rha-C10-C10)···(Rha-C10-C10) and (b) (Rha-C10-C10)···water for all of the systems studied. Refer to the text for more details.

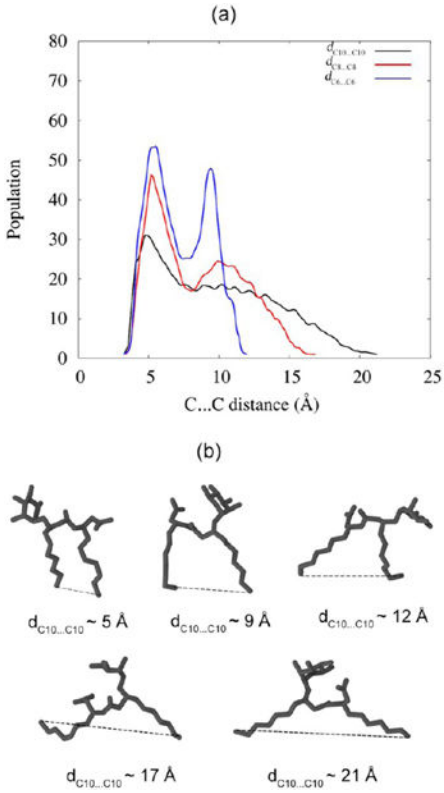

Figure 10.

(a) Population distribution of the C−C distance for aggregate N25. Refer to Scheme 1 for carbon atom numbering. (b) Representative structures of Rha-C10-C10 from the aggregates showing the different alignments of alkyl chains.

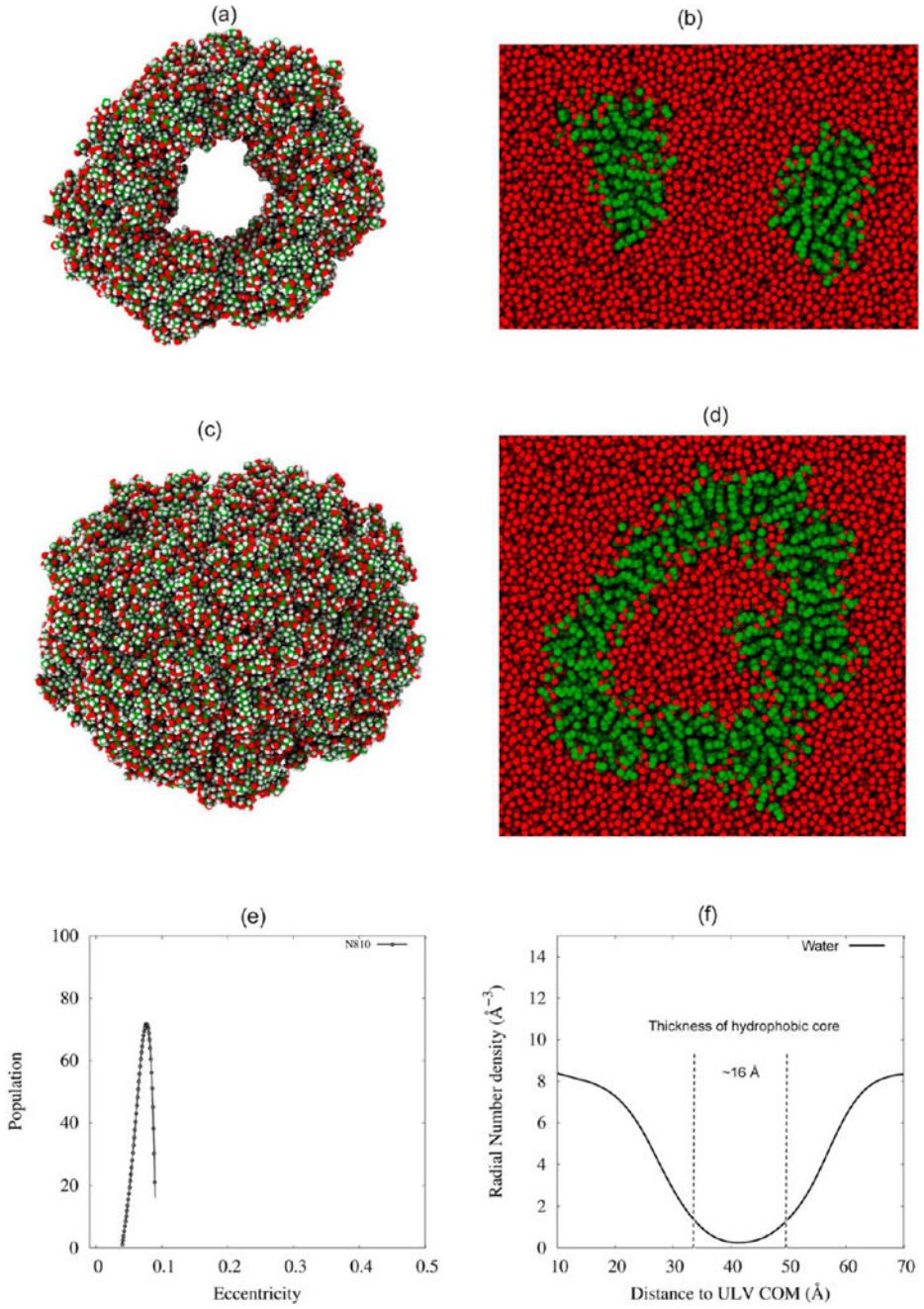

Figure 11.

Snapshot of the (a) torus aggregate and (c) unilamellar vesicle obtained from MD simulations. Cross-sectional view of the (b) torus aggregate and (d) unilamellar vesicle in water. (e) Population distribution of eccentricities of the ULV. (f) Density of the water molecule.

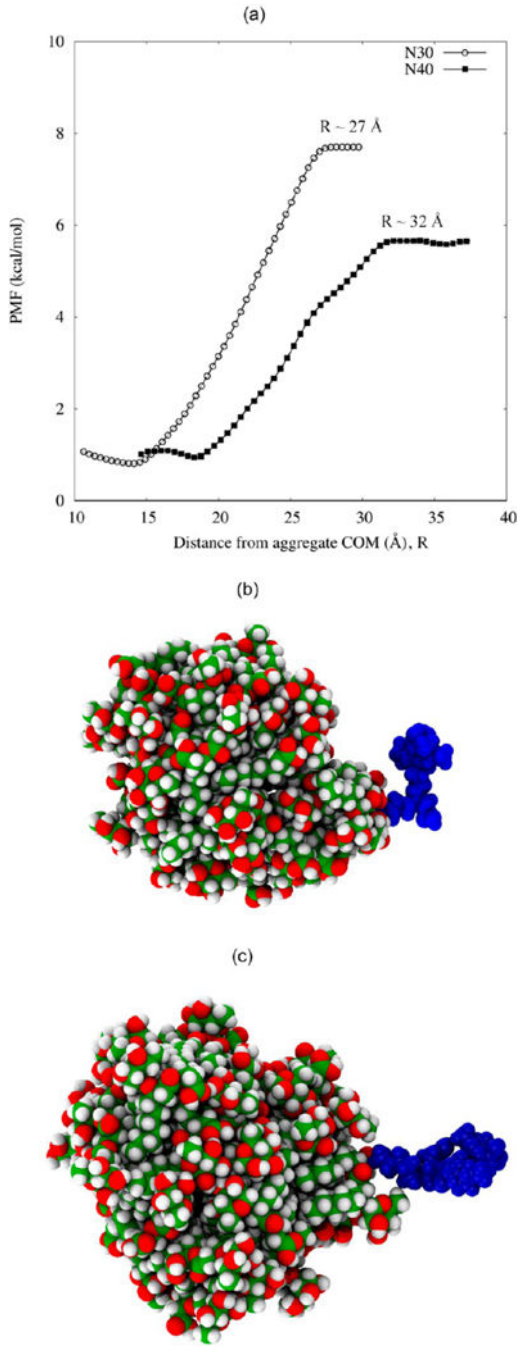

Figure 12.

(a) Potentials of mean force calculated along the reaction coordinate for a Rha-C10-C10 molecule pulled away from the COM of the rest of the aggregate. Representative snapshot of a monomer's escape from (b) N30 and (c) N40, i.e., the monomer leaving the aggregate.

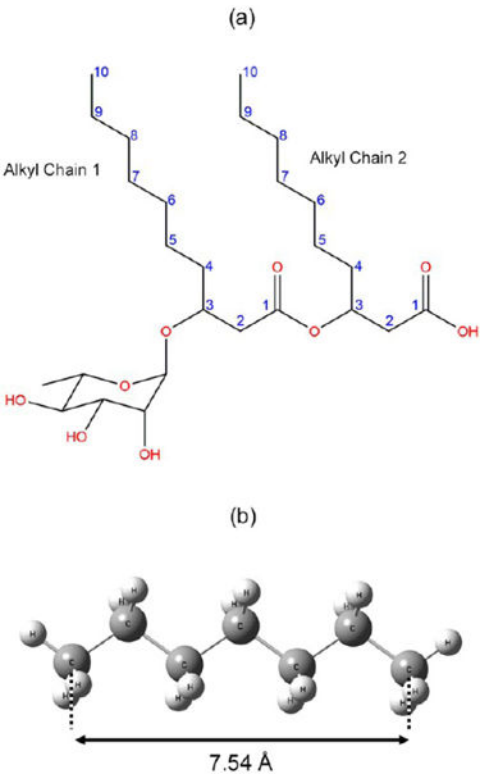

Scheme 1.

(a) Chemical Structure of Monorhamnolipid Rha-C10-C10 with Atom Numbering of the Alkyl Chains and (b) Length of an All-*trans* Seven-Carbon Alkane

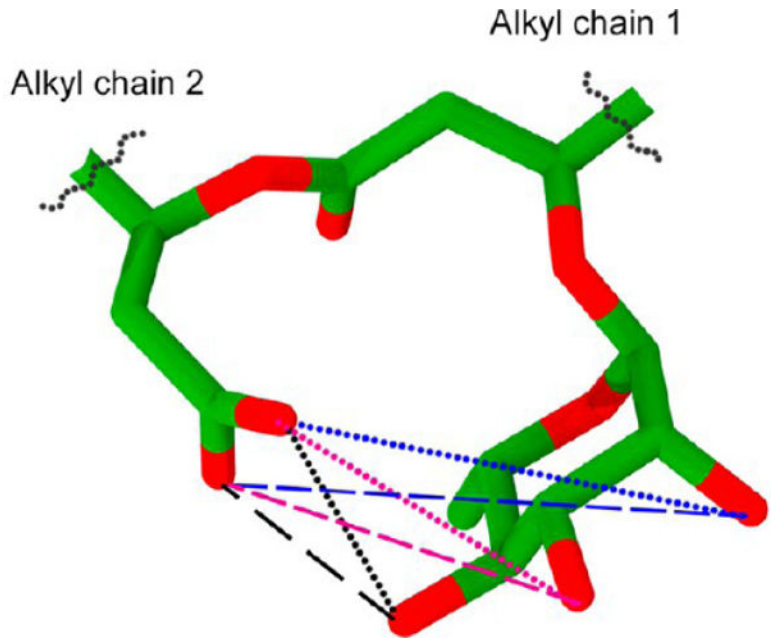

Scheme 2.

Cartoon Representation of All Possible H-Bonding Interactions between Carboxylic Groups and Rhamnose Hydroxyl Groups in Rha-C10-C10[a]

[a]The alkyl chains are not shown for the purpose of clarity.

Table 1

System Configurations for MD Simulations of Rha-C10-C10 Surfactants in Aqueous Solution

no. of Rha-C10-C10 molecules	no. of water molecules	total no. of atoms	box size (nm^3)	effective concn (mM)	simulation time (ns)
5	31847	95512	10 × 10 × 10	8.3	22
10	31544	95462	10 × 10 × 10	16.6	25
20	31247	95401	10 × 10 × 10	33.2	25
25	31079	95312	10 × 10 × 10	41.5	37
30	30946	95328	10 × 10 × 10	49.8	36
40	30638	95234	10 × 10 × 10	66.4	34
50	30054	94312	10 × 10 × 10	83.0	61
60	29740	94200	10 × 10 × 10	99.6	61
80	29399	94837	10 × 10 × 10	132.8	35
100	28352	93356	10 × 10 × 10	166	59
285	99908	323379	15 × 15 × 15	140.2	32
810	86003	325239	15 × 15 × 15	398.4	32

Table 2

Micellar Aggregate Information

no. of Rha-C10-C10 molecules	major aggregate size	minor aggregate size
5	5	N/A
10	10	N/A
20	20	N/A
25	25	N/A
30	30	N/A
40	40	N/A
50	42	8
60	44	16
80	N/A	N/A
100	N/A	N/A
285	285[a]	N/A
810	810[b]	N/A

[a]Torus-like aggregate.

[b]Unilamellar vesicle.